Fast bound pool fraction mapping by means of steady-state magnetization transfer saturation using single-shot echo planar imaging

Journal:	*Magnetic Resonance in Medicine*
Manuscript ID	MRM-18-19687.R1
Wiley - Manuscript type:	Full Paper
Date Submitted by the Author:	15-Mar-2019
Complete List of Authors:	Battiston, Marco; University College London, Queen Square MS Centre, Department of Neuroinflammation, UCL Queen Square Institute of Neurology Schneider, Torben; Philips Healthcare United Kingdom, Grussu, Francesco; University College London, Queen Square MS Centre, Department of Neuroinflammation, UCL Queen Square Institute of Neurology; University College London, Centre for Medical Image Computing, Department of Computer Science Yiannakas, Marios; University College London, Queen Square MS Centre, Department of Neuroinflammation, UCL Queen Square Institute of Neurology Prados, Ferran; University College London, Queen Square MS Centre, Department of Neuroinflammation, UCL Queen Square Institute of Neurology; University College London, Centre for Medical Image Computing, Department of Computer Science; Universitat Oberta de Catalunya De Angelis, Floriana; University College London, Queen Square MS Centre, Department of Neuroinflammation, UCL Queen Square Institute of Neurology Wheeler-Kingshott, Claudia; University College London, Queen Square MS Centre, Department of Neuroinflammation, UCL Queen Square Institute of Neurology; University of Pavia, Department of Brain and Behavioural Sciences; IRCCS Mondino Foundation, Brain MRI 3T Research Centre Samson, Rebecca; University College London, Queen Square MS Centre, Department of Neuroinflammation, UCL Queen Square Institute of Neurology
Research Type:	Magnetization transfer < Technique Development < Technical Research
Research Focus:	Brain < Neurological

Fast bound pool fraction mapping via steady-state magnetization transfer saturation using single-shot EPI

Marco Battiston[1], Torben Schneider[2], Francesco Grussu[1,3], Marios C. Yiannakas[1], Ferran Prados[1,4,5], Floriana De Angelis[1], Claudia A.M. Gandini Wheeler-Kingshott[1,6,7], Rebecca S. Samson[1]

(1) Queen Square MS Centre, Department of Neuroinflammation, UCL Queen Square Institute of Neurology, Faculty of Brain Sciences, University College London, London, United Kingdom

(2) Philips UK, Guildford, Surrey, UK

(3) Centre for Medical Image Computing, Department of Computer Science, University College London, London, UK

(4) Centre for Medical Image Computing, Department of Medical Physics and Biomedical Engineering, University College London, London, UK

(5) Universitat Oberta de Catalunya, Barcelona, Spain

(6) Department of Brain and Behavioural Sciences, University of Pavia, Pavia, Italy

(7) Brain MRI 3T Research Centre, IRCCS Mondino Foundation, Pavia, Italy

Word count: ~5500

Running title: Fast BPF mapping with EPI

Key words: quantitative magnetization transfer, steady-state, two-pool model, myelin, bound pool fraction, EPI

Corresponding author: Marco Battiston (Email address: marco.battiston@ucl.ac.uk; Phone number: +44 (0)77 4627 8361; Mailing address: Russell Square House, 10-12 Russell Square, London WC1B 5EH, UK)

Abstract

Purpose: To enable clinical applications of quantitative Magnetization Transfer (qMT) imaging by developing a fast method to map one of its fundamental model parameters, the bound pool fraction (*BPF*), in the human brain.

Theory and Methods: The theory of steady-state MT in the fast-exchange approximation is used to provide measurements of *BPF*, and bound pool transverse relaxation time (T_2^B). A sequence that allows sampling of the signal during steady-state MT saturation is used to perform *BPF* mapping with a 10 minutes long fully EPI-based MRI protocol, including inversion recovery T_1 mapping and B_1 error mapping. The approach is applied in six healthy subjects and one multiple sclerosis patient, and validated against a single-slice full qMT reference acquisition.

Results: *BPF* measurements are in agreement with literature values using off-resonance MT, with average *BPF* of 0.114(0.100-0.128) in white matter and 0.068(0.054-0.085) in grey matter. Median voxel-wise percentage error compared to standard single slice qMT is 4.6%. Slope and intercept of linear regression between new and reference *BPF* are 0.83(0.81-0.85) and 0.013(0.11–0.16). Bland-Altman plot mean bias is 0.005. In the multiple sclerosis case, the *BPF* is sensitive to pathological changes in lesions.

Conclusion: The method developed provides accurate *BPF* estimates and enables shorter scan time compared to currently available approaches, demonstrating the potential of bringing myelin sensitive measurement closer to the clinic.

Introduction

The bound pool fraction (*BPF*), also known as the macromolecular proton fraction or pool size ratio, is a key biophysical parameter for the quantitative description of the magnetization transfer (MT) effect in biological tissues. The *BPF* has its foundation in the so-called two-pool model [1], where hydrogen nuclei are modelled as belonging to two different pools: the free pool, describing mobile protons (such as those of water molecules), and the bound pool for semisolid protons (such as those bound to macromolecules). The two pools exchange magnetization via cross-relaxation and chemical exchange [2]. Given the two-pool model, the *BPF* refers to the fractional size of the bound pool, and conveys information on the macromolecular content of tissues [3].

A number of studies, both in ex vivo human tissue [4] and animal models [5-9], have shown correlations between *BPF* and myelin content. These findings suggest that the *BPF* could be a relevant biomarker in demyelinating disorders such as multiple sclerosis, sparking interest in developing methods that can extract this parameter in vivo.

The standard way to estimate the *BPF* in vivo requires the acquisition of a number of images obtained at different levels of magnetization saturation ('MT weighting') for the bound pool, used to fit the two-pool model equations. This provides the following model parameters: free and bound longitudinal relaxation times $T_1^{F,B}$, free and bound transverse relaxation times $T_2^{F,B}$, exchange rate R and the aforementioned *BPF*. A common practice is to separately estimate the T_1 of the tissue under investigation, the observed T_1 (T_1^{obs}), and then combine it with the fundamental parameters of the two-pool model [1], and explicitly correct for field in-homogeneities using measures of B_1 and B_0 variation.

Such an approach, generally termed quantitative Magnetization Transfer (qMT) imaging, has been widely performed in research centres to successfully study healthy and pathological brain tissue, but has so far not been translated to clinical settings as a non-invasive tool to characterize diseases. The major reasons for such a lack of translation are: (*i*) the duration of the acquisition protocol necessary to accurately and precisely quantify model parameters (in the order of 30 minutes), and (*ii*) the complexity of the analysis to robustly invert the model.

The need for clinically viable qMT with shorter scan times has promoted the development of approximated, and thus faster, approaches [10-12]. Existing fast methods rely on fixing some of the unknown model parameters (such as T_2^F, T_2^B, and the exchange rate R) to population average values, while leaving the *BPF* as a free parameter to be estimated from the data. This allows the reduction of the number of images to be acquired, with consequent shortening of the imaging protocol. While an initial study on a small cohort of multiple sclerosis patients has shown that such a practice does not compromise the *BPF* sensitivity to disease [13], more comprehensive and deeper investigations are desirable to thoroughly assess the impact of such a single parameter qMT fitting on quantitative

interpretations, especially in disease conditions, where models already represent gross simplifications of the underlying tissue state.

In this study, we develop a new approach for fast *BPF* mapping without the need for fixed parameters. Hard constraints on model parameters adopted in previous methods are avoided by using simplifications of the general two-pool model that can be invoked under: (*i*) steady-state conditions, and (*ii*) "*fast exchange*" regime conditions. Rather than using hard constraints on model parameters, the fast exchange hypothesis enables practical approximations for those model parameters that are fixed to predetermined a priori values in single point qMT methods. A single-shot spin echo (ssh-SE-) EPI sequence is adapted to enable the acquisition of steady-state MT contrast, allowing robust estimation of the *BPF* with an acquisition time of under 10 minutes.

Theory

In the following section, we outline the relevant theory behind the proposed new, simplified model for qMT imaging.

Typically, an MT experiment consists of the repetition of two fundamental blocks: (*i*) a saturation block (which can be implemented in several ways, e.g. with off-resonance pulses, inversion pulses, or on-resonance pulses), that disrupts the system equilibrium; followed by (*ii*) a free-evolution block, where the spin system recovers towards equilibrium. The modelling of both events is provided by the coupled Bloch equations of a two-pool system, consisting of free (indicated by superscript F) and bound (indicated by superscript B) proton pools [1], currently considered as the standard model for describing the conventional MT effect.

To provide an analytical expression for the longitudinal magnetization of the free pool M_z^{F}, (proportional to the measured signal in the MT experiment), it is convenient to express the saturation event as an instantaneous loss of longitudinal magnetization in both pools [14, 15], condensed into the fractional saturation parameters:

$$\delta_F = 1 - \frac{M_z^F(t_{sat}^+)}{M_z^F(t_{sat}^-)}$$

$$\delta_B = 1 - \frac{M_z^B(t_{sat}^+)}{M_z^B(t_{sat}^-)} \qquad [1]$$

where M_z^{F}, M_z^{B} refer to the longitudinal magnetization of the free and bound pools respectively, and t_{sat}^-, t_{sat}^+ refer to the time instants before and after the 'instantaneous' saturation event. The free-evolution period after an arbitrary saturation $\delta_{\mathrm{F,B}}$ is described by the two-pool equations:

$$\begin{bmatrix} \frac{dM_z^F(t)}{dt} \\ \frac{dM_z^B(t)}{dt} \end{bmatrix} = \begin{bmatrix} -\left(k_{FB} + R_1^F\right) & k_{FB} \\ k_{BF} & -\left(k_{BF} + R_1^B\right) \end{bmatrix} \begin{bmatrix} M_z^F(t) \\ M_z^B(t) \end{bmatrix} + \begin{bmatrix} R_1^F M_0^F \\ R_1^B M_0^B \end{bmatrix} = AM(t) + B$$

[2]

for any $t>t_{sat}^{+}$, with $M_z^i(t_{sat}^{+})=1-\delta_{F/B}M_z^i(t_{sat}^{-})$, where i=F,B. In equation 2, M_0^F and M_0^B refer to the equilibrium magnetization of the free and bound pools, R_1^F and R_1^B their longitudinal relaxation rates (inverse of relaxation times), and $k_{FB}=RM_0^B$ and $k_{BF}= RM_0^F$ are the forward and backward exchange rate, with R being the fundamental exchange rate, weighted by the respective pool sizes in each direction. During the system evolution, transverse components are usually discarded, as in the free evolution transverse magnetization is decoupled from the longitudinal one and assumed to disappear through relaxation and spoiling [16]. The *BPF* is defined as: $M_0^B \big/ M_0^B + M_0^F = k_{FB} \big/ k_{FB} + k_{BF}$. According to Equation 2, the system evolves with an exponential law governed by two rates [14], i.e. the eigenvalues of matrix A:

$$\lambda_1 = \frac{1}{2}\left[R_1^B + k_{BF} + R_1^F + k_{FB} - \sqrt{\left(R_1^F + k_{FB} - R_1^B - k_{BF}\right)^2 + 4k_{FB}k_{BF}}\right]$$

$$\lambda_2 = \frac{1}{2}\left[R_1^B + k_{BF} + R_1^F + k_{FB} + \sqrt{\left(R_1^F + k_{FB} - R_1^B - k_{BF}\right)^2 + 4k_{FB}k_{BF}}\right]$$

[3]

With the smaller rate λ_1 representing the observed longitudinal relaxation rate of the system, $\lambda_1=R_1^{obs}$.

A pulsed steady-state, in which M_z^F and M_z^B behave periodically, is reached after several repetitions of blocks (*i*) and (*ii*), meaning that the magnetisation at each time $M_z^{F/B}(t_{sat}^{-})$ returns to the same state as the previous iteration. Defining T as the off-resonance pulse repetition time of the MT experiment, M_z^F at the steady-state, denoted as M_{ss}, is given by [17]:

$$\frac{M_{ss}}{M_0^F} = \frac{1 - e^{-\lambda_1 T} + D\delta_B\left(\frac{1 - e^{-(\lambda_2 - \lambda_1)T}}{1 - (1 - \delta_B)e^{-\lambda_2 T}}\right)}{1 - \left[1 - \delta_F - K(\delta_B - \delta_F)\left(\frac{1 - e^{-(\lambda_2 - \lambda_1)T}}{1 - (1 - \delta_B)e^{-\lambda_2 T}}\right)\right]e^{-\lambda_1 T}}$$

[4]

where coefficients K and D are defined as:

$$K = \frac{k_{FB} + R_1^F - \lambda_1}{\lambda_2 - \lambda_1}$$

$$D = \frac{R_1^F - \lambda_1}{\lambda_2 - \lambda_1}$$

[5]

Quantitative MT studies on human brain in vivo have shown that the two-pool model is characterized by conditions of *fast exchange*, expressed by the condition:

$$|\varepsilon| = \left| \frac{R_1^B - R_1^F}{k_{FB} + k_{BF}} \right| \ll 1$$

[6]

Equation 6 states that the differential relaxation between pools during the exchange time is small. Such condition has been used in various derivations of qMT models [18-20]. In line with those approaches, the condition given by equation 6 can be exploited to obtain a useful expression for equation 4, considering the following approximations for $\boldsymbol{\lambda}_1$ and $\boldsymbol{\lambda}_2$ in the fast exchange regime:

$$\lambda_1 \approx R_1^F + \varepsilon k_{FB}$$

$$\lambda_2 \approx k_{FB}(1 - \varepsilon) + k_{BF}(1 + \varepsilon) + \lambda_1$$

[7]

which lead to

$$D \approx 0$$

$$K \approx \frac{k_{FB}}{k_{FB} + k_{BF}} = BPF$$

[8]

Additionally, under the condition $T > 3/(\lambda_2 - \lambda_1)$, the exponential terms $e^{-\lambda_2 T}$ and $e^{-(\lambda_2 - \lambda_1)T}$ are negligible (i.e. $e^{-\lambda_2 T} \approx e^{-(\lambda_2 - \lambda_1)T} \approx 0$), giving:

$$\frac{M_{ss}}{M_0^F} = 1 - \frac{\delta_F + BPF(\delta_B - \delta_F)e^{-\lambda_1 T}}{1 - [1 - \delta_F - BPF(\delta_B - \delta_F)]e^{-\lambda_1 T}}$$

[9]

For MT experiments via off-resonance saturation, the frequency offset Δ of the saturation can be chosen so that $\delta_F \sim 0$, resulting in:

$$\frac{M_{ss}}{M_0^F} = 1 - \frac{\delta_B BPF e^{-\lambda_1 T}}{1-(1-\delta_B BPF)e^{-\lambda_1 T}}$$

[10]

In equation 10, δ_B is dependent on saturation parameters (offset frequency Δ, and saturation flip angle θ), bound pool absorption lineshape g, commonly assumed to be super-Lorentzian [21, 22], and bound pool transverse relaxation time T_2^B.

According to Equation 1, for the calculation of δ_B the value of M_z^B at the end of the off-resonance saturation pulse ($M_z^B(\tau)$) is needed. This is obtained by numerically solving the full Bloch equations over the whole duration of the off-resonance pulse time course $\omega_1(t) = \gamma B_1(t)$, assuming that no relaxation and exchange takes place during saturation:

$$\begin{bmatrix} \frac{dM_x^F(t)}{dt} \\ \frac{dM_y^F(t)}{dt} \\ \frac{dM_z^F(t)}{dt} \\ \frac{dM_z^B(t)}{dt} \end{bmatrix} = \begin{bmatrix} -\frac{1}{T_2^F} & 2\pi\Delta & 0 & 0 \\ -2\pi\Delta & -\frac{1}{T_2^F} & \omega_1(t) & 0 \\ 0 & -\omega_1(t) & -\left(R_1^F + k_{FB}\right) & k_{BF} \\ 0 & 0 & k_{FB} & -\left(R_1^B + k_{BF} + \pi\omega_1^2(t) g_{\boldsymbol{B}}\right) \end{bmatrix} \begin{bmatrix} M_x^F(t) \\ M_y^F(t) \\ M_z^F(t) \\ M_z^B(t) \end{bmatrix} + \begin{bmatrix} 0 \\ 0 \\ R_1^F \\ R_1^B \frac{BPF}{1-BPF} \end{bmatrix}$$

[11]

where $1/T_2^F$, R_1^F, R_1^B, $k_{BF,}$ and k_{FB} are all set to zero. Equation 11 is solved for the time instant $t=\tau$, with initial condition $M_x^F(0)= M_y^F(0)=0$, $M_z^F(0)=1$, $M_z^B(0)=BPF/1-BPF$.

BPF and T_2^B can therefore be extracted using Equations 10 and 11, by sampling the magnetization M_{ss} for various combinations of Δ and θ, provided that: (*i*) steady-state is reached; (*ii*) long T are used (to satisfy $T > 3(\lambda_2 - \lambda_1)$); and (*iii*) a measure of $\lambda_1=R_1^{obs}$ is available. Importantly, equation 10 is much more tractable compared to numerical integration of equation 2, simplifying the implementation of qMT fitting, and reduces the number of model parameters to estimate to 2, *BPF* and T_2^B, rather than the4 model parameters of the more commonly used qMT models.

Methods

MR Sequence

Time efficient sampling of the steady-state magnetization is achieved using the sequence shown in Figure 1. The pulsed steady-state is attained with an initial period of saturation, where a single off-resonance pulse of duration τ and flip angle θ is repeated every T, i.e. the pulse repetition time. The time needed to reach the steady state depends on sequence parameters τ, θ and T, as well as the fundamental parameters of the tissue under investigation. For brain tissue the T required to fulfil the conditions of equation 7 is on the order of 120-150ms [19, 23, 24], as also shown in Supporting Figure S2, therefore a saturation period of ~4s is sufficient (i.e. around 30 off-resonance pulses). The steady-state is maintained during the acquisition, by continuously interleaving imaging pulses with off-resonance saturation pulses.

Given the long pulse repetition time proposed here, the maximum time efficiency for the sequence is achieved when the whole k-space is acquired between the saturation pulses in steady-state, hence by using ssh-EPI readouts. Long recovery times $T_{rec} \geq 5/R_1^{obs}$ are not required between sequence repetitions, as the subsequent preparation will force the system into a new steady-state and is independent from the initial state of the magnetization vector.

Simulations

The effect of sequence parameters τ, θ, T and number of data points M on BPF and T_2^B estimates is investigated through simulations.

Full two-pool model equations are used to generate steady-state signals for physiologically plausible values of tissue parameters. For white matter tissue: BPF = 0.13(0.02); T_2^F = 34.1(8.6) ms; T_2^B = 10(1)μs; k_{FB} = 2.87(0.51)s^{-1}; T_1^{obs} = 1.00(0.19) s. For grey matter tissue: BPF = 0.08(0.01); T_2^F =52.11(13.1) ms; T_2^B =9(1) μs; k_{FB}=1.92(0.44) s^{-1}; T_1^{obs} = 1.38(0.25) s. These values were obtained from initial quantitative MT experiments in the healthy human brain. Simulated signal are then fitted by Equation 10, assuming that there are no errors on the R_1^{obs} inserted in the model (i.e. the simulated longitudinal relaxation rate is used for the fitting).

Errors on parameter estimates are evaluated for 6 different protocols, whose details are reported in Table 1. Briefly, four protocols are labelled as long protocols (L1, L2, L3, L4): they each consist of 20 data points, and the effect of different T is considered; one protocol is labelled as short (S1) where the effect of having less data points is investigated, and the final protocol is labelled as optimized (O1).

Protocol O1 was obtained by performing computational optimisation of the Cramer-Rao lower bounds of model parameters BPF and T_2^B using a self-organizing migratory algorithm (SOMA) [25, 26], similarly to a previous study [27].

For all protocols, off-resonance saturation is performed with a Fermi shaped RF pulse.

In vivo acquisition

Six healthy subjects are scanned using a 3T Philips Ingenia CX MRI (Philips Healthcare, Best, The Netherlands) and a 32-channel head coil, after having given informed consent. The imaging protocol consists of: (*i*) MT-weighted acquisition using the sequence displayed in figure 1, (*ii*) T_1 mapping protocol, (*iii*) B_1 mapping protocol, and (*iv*) a 3D-T_1-weighted anatomical scan. Acquisitions to be used for quantitative purposes (*i*), (*ii*) and (*iii*) are all performed using a single-shot spin echo ssh-SE-EPI readout.

For the MT-weighted acquisition the optimized protocol O1 from table 1 is chosen, based on its superior performance in simulations. Off-resonance saturation is performed using a Fermi RF pulse, defined by the shape parameters $t_0=2.7*10^{-3}$ and $a=0.18*10^{-3}$ [28], with duration τ=8ms, bandwidth=769 Hz, played out at two 2 different amplitudes $B_{1,max}$=10.8μT and 7.9 μT. Two additional acquisitions are added at Δ=96kHz, therefore exhibiting no MT-weighting, to be used as a normalization factor (M_0 in Equation 10). The imaging parameters are: *FOV*=224x224x120 mm^3, resolution 2 mm isotropic, N_s=60, acquisition matrix size=112x110, SENSE factor = 2, no partial Fourier imaging, EPI train length=55, *TR*=16890 ms, *TE*=38 ms, and T_{rec}=1800 ms. Total scan time is 3:56 sec. For T_1 mapping, an inversion recovery (IR)-EPI sequence is used. Non-spatially selective adiabatic inversion is performed to prepare magnetization, and a slice-shuffling mechanism [29] in the acquisition is used to produce different inversion times without *TR* increases. Adiabatic inversion is performed using a hyperbolic secant pulse, defined by the shape parameter μ=5, and β=818.8 rad/s [30], with duration 9.78ms, maximum amplitude 13.1 μT, and bandwidth 1302 Hz. Fifteen inversion times are sampled from 50ms to 1730ms, equally spaced by 120ms. *TR*=6735ms, *TE*=43ms, multi band acceleration factor=2, and with all the other imaging parameters the same as for the MT-weighted sequence. Total scan time is 3:36sec. For B_1 mapping, a Double-Angle method (DAM) [31] is used. Parameters are: α_1\ α_2=60\12°, TR=12000ms, TE=38ms, two signal averages, and with all other imaging parameters the same as for the MT-weighted sequence. Total scan time is 1:12sec.

Details of preparation and imaging pulses used in the in vivo acquisition are reported in Supporting Information Figure S1.

A sagittal 3D-T1-weighted scan (FOV=256x256x176mm^3, resolution=1mm isotropic, TR=7ms, TE=3.2ms, flip angle=8°, compressed sense factor=6) is added to the MRI protocol to allow regional characterization of the tissue parameter estimates (scan time of approximately 2 minutes).

In order to validate parameter values obtained with the new, fast approach developed here, in one subject a more conventional qMT approach is performed with a single-slice, geometrically matching the central slice of the acquired FOV of the steady-state approach.

MT saturation is achieved with a train of off-resonance saturation pulses, followed by a ssh-SE-EPI-readout (same imaging parameters used for the newly developed full coverage acquisition). A recovery time of 6s is inserted between repetitions of different MT preparation, to allow full longitudinal magnetisation recovery. While being extremely time-consuming and therefore not feasible in a clinical setting, such an approach represents the ideal MT experiment, where MT preparation is separate from data readout and not affected by imaging pulses. Moreover, in a single slice single-shot acquisition any additional unwanted MT-weighting due to multiple excitations is avoided. Therefore, such an approach can considered as a reliable reference. MT saturation parameters are: 30 sinc-gaussian pulses of 15 ms duration, separated by 5 ms gap, for 18 different combinations of (Δ (in kHz) ,θ (in degrees)): (2,700), (2.5,700), (3,700), (2/1400), (2.5/1400), (3/1400), (2.7/700), (2.7/700), (2.7/1400), (4,1400), (5,1400), (12,1400), (12,1400), (2,1100), (2.3,1100), (3,1100), to sufficiently sample the Z-spectrum. The maximum bandwidth and amplitude for the sinc-gaussian pulse was 106Hz and 11.31μT. Four images without MT-weighting (Δ,θ=96kHz,100°) are also acquired for normalization purposes. Two signal averages are used for each data point.

In order to assess the feasibility of using the method to investigate demyelination in vivo, a secondary progressive multiple sclerosis (SPMS) patient (male, 61 years old, EDSS=6.0) is scanned with the quantitative protocol used in the cohort of healthy subjects. In addition to the quantitative scans, a set of co-localized conventional scans are added. These consist of: (*i*) an axial T_1-weighted turbo spin echo scan (resolution 1x1x2 mm^3, TR=625 ms, TE=10 ms, compressed sensing factor=2; scan time 08:15 sec); (*ii*) a 3D T_2-weighted turbo spin echo scan (resolution 1x1x1 mm^3, refocusing flip angle=35°, TR=2500ms, TE=250ms, turbo factor=133, scan time 4:22 sec); (*iii*) a 3D FLAIR (resolution 1x1x1 mm^3, refocusing flip angle=40 °, TR=5000 ms, TE=350 ms, turbo factor 177, TI=1650 ms, compressed sensing factor=8, scan time 6:35sec); and the same 3D T_1-weighted scan performed in the healthy subjects.

In vivo image analysis

Data are analysed using in-house Matlab r2015 software (The Mathworks, Inc., Natick, MA). A non-linear least squares approach is used to fit magnitude IR data, assuming a standard mono-exponential model with perfect inversion of magnetization following the adiabatic pulse. A voxel-wise $\lambda_1 = \frac{1}{T_1}$ measure is then inserted into Equation 10, to estimate *BPF* and T_2^B, again via non-linear least squares fitting. The percentage B_1 variation obtained from the DAM acquisition is used to correct for the actual flip angle of the MT saturation pulses in the computation of δ_B, which encapsulates the unknown parameter T_2^B. A super-Lorentzian lineshape is assumed for the macromolecular pool, and a discretizing step of 120μs is used for the calculation of δ_B, via numerical integration of equation 11.

For the single-slice qMT dataset, the full two-pool model equations are fitted to magnitude data, using the numerical approach termed 'minimal approximation MT model' [16, 27]. The same T_1 map and B_1 map of the MT steady-state dataset are used to inform the model and correct for B_1 errors. A super-Lorentzian lineshape is again assumed, and a discretizing step of 120μs for the numerical integration of Bloch equations is used.

A voxel-wise linear regression, correlation coefficient R, and Bland-Altman plot are used to compare *BPF* maps between single-slice qMT and steady state full coverage MT in the same (central) slice. Average regional values are instead reported for all the subjects scanned with the steady-state MT approach. The 3D-T_1-weighted scan was used for segmentation to define the different tissue types: white matter (WM), cortical grey matter (cGM), deep grey matter (dGM) and brain stem (BS). Automatic definition of regions-of-interest (ROI) is performed using the GIF segmentation tool [32] after rigidly registering the 3D-T_1-w volume to the subject-specific EPI space with the NiftyReg package. Finally, we evaluate contrast-to-noise ratio (*CNR*) between WM and cGM in the *BPF* map as:

$$CNR = \frac{\overline{BPF}_{WM} - \overline{BPF}_{cGM}}{\sqrt{(\langle BPF\rangle_{WM})^2 + (\langle BPF\rangle_{cGM})^2}} \quad [12]$$

where $\overline{BPF}_{WM,cGM}$ refer to the whole brain WM and cGM mask *BPF* mean, and $\langle BPF\rangle_{WM,cGM}$ to their respective standard deviations.

For the SPMS case, the same pipeline described for the healthy volunteers is followed. In addition, a lesion mask is outlined manually. Two types of lesion are defined: lesions that appear on all the modalities, as hypo-intense on both T_1-weighted scans and as hyper-intense on both T_2-weighted scans (i.e. *hypo-intense* lesions, or otherwise known as "black holes"); and lesions that appear as hyper-intense on the T_2-weighted scans but do not show any alteration in at least one of the T_1-weighted scans (e.g. *hyper-intense* lesions). Average regional *BPF* values are reported, for the two lesion types, as well as normal appearing WM, cGM, dGM, and BS, after removing voxels marked as lesional.

Results

A fast and efficient sequence for whole brain qMT in less than 10 minutes was successfully implemented for in vivo applications at 3T.

The effects of sampling (M, τ, T, θ, Δ) and *SNR* on estimates of model parameters *BPF* and T_2^B are shown in Figure 2, from simulation experiments. The *BPF* shows large bias when the condition on the pulse repetition time is not met, even at high *SNR* and acquiring a large number of data points (e.g.

median percentage error on *BPF* is 20.5% for protocol L1 at *SNR*=300). Errors on *BPF* are greatly reduced for protocols where $T \geq 150$ms (such as protocols L3, L4, S1, O1), regardless of the number of data points or the adoption of an optimized sampling scheme (at *SNR*=300, maximum median error on *BPF* is -2.3% for protocol L4). Conversely T_2^B is less sensitive to the constraint on the pulse repetition time, but shows a stronger dependency on *SNR* and number of data points compared to *BPF*. At a realistic *SNR*=30 for a ssh-SE-EPI acquisition in the brain, variability of T_2^B error is more than three times higher than variability on *BPF* (inter-quartile range of T_2^B error = -25.5%\18.9%; inter-quartile range of *BPF* error = -10.1%\3.3%). Protocol optimization effectively improves the precision of T_2^B, with smaller benefits on precision and accuracy of *BPF*, despite the acquisition of less data points: protocol O1 for in vivo imaging would take 50% of the time needed for long protocols L3 and L4, providing similar parameter estimates. Importantly, a better estimation of T_2^B reduces the bias on *BPF* at all the *SNR* levels investigated (median of *BPF* error: -2.0%\-1.3%\-1.8%, for *SNR*=300,30 and 15 respectively with the optimized protocol O1).

Examples of errors in the simulated parameters maps are shown in Figure 3, where a long protocol (L3), a short protocol (S1) and an optimized protocol (O1) are compared, essentially reporting the results of Figure 2 in a more intuitive form. Simulations confirm that *BPF* can be robustly estimated with a limited number of data points, especially following protocol optimization, with negligible bias even at low *SNR* regime. According to results from simulations, protocol O1 is selected for in vivo imaging.

Examples of parameter maps in a representative subject are shown in Figure 4, where T_1^{obs}, *BPF* and T_2^B are visualized over three different slices. The *BPF* depicts the expected contrast between WM, highly myelinated, and GM, with remarkably less myelin content. On the other hand, less clear delineation between structures is visible in the T_2^B maps, confirming the reduced WM/GM contrast provided by this parameter and its marked heterogeneity in WM, as previously reported [10, 33, 34]. An example of *BPF* over the whole *FOV* is shown in Figure 5 for another subject. WM/GM contrast is consistent throughout the volume, and the correction using B_1 maps mitigates the spatial inhomogeneity due to the variations of the transmit field. Axial views of the *BPF* map are shown in Supporting Information Figure S4.

Average parameter values in all subjects are reported in Table 2, for 4 different ROIs: cGM, dGM, WM and BS. Tissue values are consistent among subjects and in line with literature values. Overall WM/cGM BPF *CNR*, average over all the subjects, is 1.47(0.12), with dGM *BPF* higher than cGM in all subjects. Population values are summarized in Figure 6, where *BPF* distributions, normalized and non-normalized, from all subjects pooled together are shown. The *BPF* differentiates between the WM and cGM well, reflected in the bi-modal distribution with two distinct peaks and clear separation.

The *BPF* mapping from steady-state MT is compared with a standard qMT acquired in one subject. Figure 7 summarizes the main results of this comparison. Despite a lower *SNR* (as no signal average is

used) and a reduced scan time, *BPF* measured using the steady-state acquisition is highly correlated with the reference *BPF* (linear correlation index R=0.85 ($p<0.01$)). Voxel-wise linear regression gives a slope of 0.83 (confidence interval 0.81-0.85), and an intercept of 0.013 (confidence interval 0.011-0.016). The Bland Altman plot provides a negligible mean bias of 0.005 for *BPF* (corresponding to 4.42% of the mean value for *BPF*) with the majority of the voxels included within the limit of agreements (-0.029 – 0.038). These findings overall suggest only a minimal bias in the *BPF* estimation, when the fast method developed here is compared with the reference single-slice acquisition. The maps show remarkably similar spatial patterns, and contrast between structures. A quantitative evaluation of the voxel wise error reveals a mild underestimation of the *BPF* when using the approach developed here, with median and 25^{th}-75^{th} percentiles of the percentage error distribution of 4.6% (-4.9%/13.1%). As expected, the other estimated parameter, T_2^B, is noisier when measured using the steady-state approach compared to the standard method, as confirmed by the comparison between parametric maps where differences between structures are reduced, and by the correlation plot, providing a lower correlation index R=0.37 ($p<0.01$), compared to *BPF* with R=0.85 ($p>0.01$). A reduced precision is confirmed by the slope of the linear regression, i.e. 0.65, with larger confidence interval (0.59-0.72), compared to the *BPF* analysis. However, the Bland Altman plot shows a minimal bias of -0.28μs compared to the reference approach, and voxel-wise error computation reveals only a slight overestimation, with median and 25^{th}-75^{th} percentiles of the percentage error distribution of -1.6% (-9%/4.4%).

The *BPF* maps derived from the scan on a MS patient are shown in Figure 8, together with the corresponding qualitative clinical scans. Several lesions are visible on the multi-contrast set of images (highlighted by arrows), and are characterized by lower *BPF* values in the corresponding quantitative maps compared to the normal appearing tissue. Average *BPF* values in the SPMS case are: 0.057 (0.023) for normal appearing cGM, 0.067 (0.020) for normal appearing dGM, 0.101 (0.022) for normal appearing WM, and 0.114 (0.035) for normal appearing BS. In the lesion mask, average *BPF* values are instead: 0.035 (0.015) for the hypo-intense lesions (total volume 1728 mm^3), and 0.052 (0.023) for the hyper-intense lesions (total volume 4904 mm^3).

Discussion

In this work, we have presented a new, fast method to map the *BPF* in the human brain at 3T. The main feature of the method resides in its efficiency: large brain coverage, with 2mm slice thickness and relatively high in plane resolution (for quantitative MRI), *BPF* maps can be obtained in less than 10 minutes. Additionally, the method distinguishes itself from other fast *BPF* mapping approaches by avoiding the need of explicitly fixing a number of model parameters, it is carried out by means of a simple MR sequence, and it enables a more computationally straightforward analysis compared to many qMT methods available.

For these reasons, we believe that such a method can promote a more widespread use of qMT imaging, especially within clinical settings, to improve our understanding of microstructural correlates of *BPF* in a much wider range of conditions, and ultimately its potential as a quantitative imaging biomarker for myelin content.

In fact, the computation of a reliable quantitative index of myelin content in vivo using MRI remains an unresolved challenge. It is now accepted that the *BPF* is not a measure purely specific to myelin. Although myelin may represent the major MT contributor, it is indeed the whole pool of macromolecules which is captured by the *BPF*. Emerging techniques, such as inhomogeneous magnetization transfer (ihMT) [35], may be better positioned to provide an index with higher specificity to myelin content than the *BPF*. However, the sensitivity to the macromolecular component of the tissue, which still provides an indirect probe to tissue myelin content, together with its quantitative nature, allowing absolute comparisons among different MRI platforms and hardware configurations, makes it a powerful parameter for characterizing white matter diseases, for example in multi-centre and/or multi-time point clinical trials.

With the long acquisition time blamed as the main limitation for qMT use, the approach developed here, offers a substantial step towards a larger use of qMT imaging methods.

The method developed efficiently exploits the fast-exchange regime approximation for steady-state MT, where off-resonance saturation is applied at long T (i.e. 150 ms), by acquiring the entire k-space between saturation pulses. This produces an MT-weighted volume per TR~15-20 seconds.

The steady-state model for *BPF* estimation is built on the same theory used for the estimation of a parameter called MT_{sat} parameter [36], which is increasingly used as a myelin-sensitive metric for its relatively simple implementation [37], despite not having any direct biophysical interpretation. The additional assumption of fast exchange and the use of long T are advantageously exploited, here, in order to remove the dependency on the transfer, while the large offset frequency removes the free pool saturation terms from the modelling. At the same time, the increase in T allows a whole k-space sampling to be fit in between saturation events, resulting in high scan time efficiency.

In general, interleaving MT preparation with full EPI readouts is not a specific feature of the method described here and more general qMT models could be used in combination with the sequence proposed, acquiring for example non-steady-state signal. However, such approach may require further optimization to ensure the feasibility of model parameter estimation with a more complex model at a generally lower MT-weighting.

We have shown that the proposed model allows robust *BPF* estimation at the typical *SNR* of ssh-SE-EPI acquisition in the human brain, while maintaining biases below 5% when compared to the most accurate approach where no assumptions are made in the modelling and the full Bloch equations are

integrated, i.e. the minimal approximation MT model. The origin of the small remaining discrepancy between predicted bias in simulation, suggesting a slight *BPF* overestimation in the steady-state approach, and in vivo comparison, showing a mild *BPF* underestimation in the steady-state approach, is not yet fully understood. Assuming the single slice qMT approach as the ground truth, unaccounted factors in simulations that could be the cause of such a mismatch are: the effect of the normalization term (via a noisy M_0 image) on the *BPF* estimation, a different interplay between B_0 errors and *BPF* estimates in the two approaches, and potential confounding factors deriving from a multi-slice acquisition (which is discussed later in this section).

Moreover, a more accurate optimization of the sampling scheme, for instance to account also for the presence of a normalizing term at finite *SNR*, or for insensitivity to B_0 errors, may help to elucidate the cause of such discrepancy and eventually mitigate the residual error compared to the ground truth, however small in the current implementation.

The method combines naturally with a T_1 measurement via IR-EPI, which can be achieved within 4 minutes of scan time by adopting adiabatic inversion, a slice shuffling mechanism and simultaneous multi-slice acceleration, allowing fast T_1 mapping with similar distortions to the MT-weighted images.

It is important to note that lack of complete magnetization inversion following the adiabatic pulse, which has previously been reported in vivo [38], introduces errors on the T_1 measurements that propagate into the BPF estimates, as shown in Supporting Information Figure S5. Strategies to minimize such errors, for example by explicitly fitting for the inversion efficiency factor in the IR-EPI data, are important to improve the accuracy of *BPF* estimates.

Single-shot SE-EPI can also be used to perform B_1 mapping via the DAM without compromising the accuracy [39]. The use of a unified single-shot EPI readout may be beneficial to enable accurate motion correction between multiple volumes acquired over time, and among different modalities (e.g. *MT*, T_1 and B_1), by enabling the use of simple 3D rigid transformations for image registration. The protocol can be complemented with an additional acquisition, with reversed polarity for the train of phase-encoding gradients, to correct for magnetic susceptibility-induced geometrical distortions [40], to which EPI is sensitive. Again, the common readout among modalities allows the use of a single additional volume to perform distortion correction for all the acquired data, with minimal increase in the total scan time.

The interference of a multi-slice readout on the MT steady-state is reduced by avoiding fat suppression pulses (which are spectral selective and therefore liable to unwanted MT-weighting), using instead the gradient reversal technique to efficiently reduce the effective thickness of the slab where fat signal is refocused [41]. In general, the long pulse repetition time T in between subsequent slice excitations is beneficial to avoid substantial build-up of additional MT-weighting from excitation pulses, causing deviation from the steady-state during the slice acquisition module. Simulations shown in Supporting Figure S3 suggest that the slice acquisition order odd-even used in this study is responsible for a mean

percentage underestimation of approximatively 12% of the *BPF*, while it does not have any appreciable impact on T_2^B estimates.

However, further investigation is required to minimize such residual effects through optimized slice ordering schemes, as well as to assess the impact of different pulse shapes and/or duration, whose choice was here made on empirical bases.

BPF estimates are in agreement with reported values in the healthy human brain from qMT using off-resonance saturation [11], with good contrast between WM and cGM. Moreover, the short scanner time required for its acquisition will be advantageous for future applications in patients, where subject compliance may be problematic and the potential for motion is higher.

The core of the approximations made to derive the signal model for MT steady-state acquisition is based on the fast-exchange condition, expressed by equation 6. While such a condition has been invoked in the derivation of several qMT models for human brain tissue, its validity in pathology has never been assessed. Studies in patient populations are necessary to understand the limits for the applicability of the approximated model to disease, as both relaxation rates $R_1^{F,B}$ and exchange rates k_{FB} and k_{BF} are expected to deviate from physiological values. However, changes in *BPF*, that are thought to occur in many pathologies, primarily imply a modification in the relative size of the two-pool system, rather than an alteration in its exchange regime. There may be, thus, room for such an approximation to hold well also in pathology.

We have provided preliminary evidence of the feasibility of such a method to study demyelination in the human brain in vivo, by including a SPMS case, where chronic lesions are present. The approximated model is able to capture the loss of myelin expected in lesions, as shown by the reduced *BPF* values in both T_2-w hyper-intense and T_1-w hypo-intense lesions compared to normal appearing tissues. Furthermore, in the single case considered, the *BPF* is lower in the *hypo-intense* lesions (mean 0.035) compared to the *hyper-intense* lesions (mean 0.052), which is consistent with the suggestion that T_1-weighted "black-hole" lesions are associated with more severe tissue disruptions compared to T_2-weighted lesions [42].

In the healthy population, tissue type distributions resemble those obtained with a state-of-the-art ihMT protocol (see figure 6 of reference [43]), with two distinct peaks for WM and cGM, and a higher *BPF* in the deep grey matter structures, e.g the thalamus, compared to cortical grey matter. The clearer separation between distributions provided by ihMT points towards the higher sensitivity of ihMT to myelin than conventional MT, however the quantitative nature of the *BPF* may be advantageous when using such a parameter to quantify changes in disease. Moreover, the steady-state MT sequence developed here could be used to perform an ihMT experiment by replacing the single offset off-resonance pulse with a rapidly switching pulse pair at opposite offset frequencies, either to carry out

quantitative studies with a more general ihMT model [44], or simply to provide an enhanced MT-weighting which could be beneficial for the fitting.

Similarly, different pulse shapes and pulse durations could provide more efficient saturation of the bound pool and therefore improve the *BPF* estimation.

Although not tested in the implementation presented in this study, further acceleration is achievable when combining the MT-weighted acquisition with a simultaneous multi-slice acquisition strategy, similarly to the IR-EPI, especially when a higher number of slices is needed.

Conclusions

A new, fast approach to map a key parameter of the quantitative MT two-pool model, e.g. the myelin-sensitive bound pool fraction (*BPF*), has been developed and applied in a cohort of healthy volunteers. The approach has the potential to be applied in a patient population in clinical studies and enable viable quantitative measurements of important microstructure features, such as macromolecular tissue content, within clinical settings.

Acknowledgements

We thank the UK Multiple Sclerosis Society, funding MB and RS, and UCL-UCLH Biomedical Research Centre for ongoing support of the Queen Square MS Centre. We also thank the following organizations/initiatives: Spinal Research (UK), Wings for Life (Austria) and Craig H. Neilsen Foundation (USA) for INSPIRED; Engineering and Physical Sciences Research Council (EPSRC EP/R006032/1, M020533/1, G007748, I027084, M020533, N018702). Department of Health's National Institute for Health Research, Biomedical Research Centres (BRC R&D 03/10/RAG0449); Guarantors of Brain post-doctoral non-clinical fellowships. This project has received funding from the European Union's Horizon 2020 research and innovation programme under grant agreement No. 634541 (funding FG).

Supporting Information

Supporting Information Figure S1. Details of imaging and preparation pulses used in the optimized in vivo acquisition: slice selective excitation pulse (a), slice selective refocusing pulse (b), off-resonance saturation Fermi pulse (c), and hyperbolic secant adiabatic inversion pulse (d). In the in vivo MT-weighted acquisition, the Fermi pulse is used at two different amplitudes (following protocol optimization), $B_{1,max}$=10.8μT and $B_{1,max}$=7.95 μT, with the same duration τ=8ms.

Supporting Information Figure S2. Fast exchange model approximations. Different exchange regimes are analysed by artificially varying k_{FB}, starting from the model parameter configuration used in the simulations section shown in Figure 3. Faster exchange regimes correspond to lower values of ε (defined by equation 6), as shown in panel a. The exchange regime measured in vivo in the single slice qMT reference acquisition (described in the methods section) is reported in all the graphs (blue dashed line, which refers to the median of the distribution within the single slice). Validity of conditions $D\approx 0$ (panel b), $K\approx BPF$ (panel c), and $e^{-(\lambda_2-\lambda_1)T}\approx 0$ for T=100ms, 150ms and 200ms (panel c) are investigated at varying ε. In panel e) the overall effect on *BPF* estimation is analysed using the sampling protocols L2, L3 and L4 of table 2 as reference, at SNR=300. The use of long T (e.g. T =150ms) allows to maintain the percentage *BPF* error below 10% even at exchange regimes characterized by ε=0.02 (compared to a measured in vivo exchange regime ε=0.012). Median and interquartile ranges are reported in simulated trends.

Supporting Information Figure S3. Effect of the multislice acquisition module on model parameter estimates. Full two-pool Bloch equations are used to simulated MT-weighted signal of the optimized protocol O1, accounting also for additional off-resonance saturation via slice selective imaging pulses of the multislice SE-EPI readout. For each slice index i=1,…,N_s, the set of offset frequencies of excitation and refocusing pulses are obtained as $\gamma G\Delta z_{t,i}$ where G is the slice selective gradient strength, and $\Delta z_{i,t}$ is the space gap between slice i and any slice t=1,..,i-1 that precedes slice i in the acquisition. The odd-even slice acquisition order used for in vivo acquisition is reproduced in the simulation, and realistic shapes are used for the imaging pulses and preparation pulses (see Supporting Information Figure S1). The approximated model proposed is used to fit the simulated data, and percentage error on *BPF* and T_2^B is evaluated at varying *SNR*. Incidental MT-weighting from imaging spin echo pulses has a severe impact on the accuracy of *BPF* estimates, while T_2^B is less affected (*odd-even* boxplots). Prior to model fitting, however, MT-weighted images are normalized to a reference image, i.e. M_0, which is acquired within the same sequence (hence similarly affected by MT-weighting via imaging pulses). The normalization with such an M_0 image greatly attenuate the error on *BPF* estimates (*odd-even normalized* boxplots), resulting in a median percentage error of 12.3%, 12.1% and 11.9% at *SNR*=300, 30 and 15 respectively.

Supporting Information Figure S4. Axial views of *BPF* maps at 2mm in plane resolution in a representative healthy subject, including B_1 correction. The total acquisition time (i.e. T_1 mapping + B_1 mapping + steady-state MT-weighted sequence, all using ssh-SE-EPI) to obtain these maps is less than 9 minutes.

Supporting Information Figure S5. Analysis of error propagation from T_1 measurements to *BPF* estimates, following imperfect inversion of the hyperbolic secant adiabatic inversion pulse used in the IR-EPI sequence. Inversion Recovery curves are simulated at varying inversion efficiency β=0.85, 0.9,

0.95 and 1, and then fitted with a standard 2-parameter (where unknown model parameters are M_0 and T_1^{obs}), and a 3-parameter model (where unknown model parameters are M_0, $T_1^{obs}=1/R_1^{obs}$, and β). The R_1^{obs} estimates obtained are then used as input in the qMT model for *BPF* and T_2^B estimation. Percentage errors are reported for both IR-EPI fitting approaches (2-parameter fitting in box a, and 3-parameter fitting in b). The optimized protocol proposed for the in vivo acquisition (O1) is used to generate simulated MT-weighted data.

References

[1] R. M. Henkelman, X. Huang, Q. S. Xiang, G. Stanisz, S. D. Swanson, and M. J. Bronskill, "Quantitative interpretation of magnetization transfer," *Magnetic resonance in medicine,* vol. 29, pp. 759-766, 1993.

[2] S. D. Wolff and R. S. Balaban, "Magnetization transfer contrast (MTC) and tissue water proton relaxation in vivo," *Magnetic resonance in medicine,* vol. 10, pp. 135-144, 1989.

[3] J. G. Sled, "Modelling and interpretation of magnetization transfer imaging in the brain," *NeuroImage,* vol. 182, pp. 128-135, 2018.

[4] K. Schmierer, D. J. Tozer, F. Scaravilli, D. R. Altmann, G. J. Barker, P. S. Tofts*, et al.*, "Quantitative magnetization transfer imaging in postmortem multiple sclerosis brain," *Journal of Magnetic Resonance Imaging,* vol. 26, pp. 41-51, 2007.

[5] V. A. Janve, Z. Zu, S.-Y. Yao, K. Li, F. L. Zhang, K. J. Wilson*, et al.*, "The radial diffusivity and magnetization transfer pool size ratio are sensitive markers for demyelination in a rat model of type III multiple sclerosis (MS) lesions," *Neuroimage,* vol. 74, pp. 298-305, 2013.

[6] X. Ou, S. W. Sun, H. F. Liang, S. K. Song, and D. F. Gochberg, "Quantitative magnetization transfer measured pool-size ratio reflects optic nerve myelin content in ex vivo mice," *Magnetic resonance in medicine,* vol. 61, pp. 364-371, 2009.

[7] J. D. Thiessen, Y. Zhang, H. Zhang, L. Wang, R. Buist, M. R. Del Bigio*, et al.*, "Quantitative MRI and ultrastructural examination of the cuprizone mouse model of demyelination," *NMR in Biomedicine,* vol. 26, pp. 1562-1581, 2013.

[8] H. R. Underhill, R. C. Rostomily, A. M. Mikheev, C. Yuan, and V. L. Yarnykh, "Fast bound pool fraction imaging of the in vivo rat brain: association with myelin content and validation in the C6 glioma model," *Neuroimage,* vol. 54, pp. 2052-2065, 2011.

[9] F. Wang, K. Li, A. Mishra, D. Gochberg, L. Min Chen, and J. C. Gore, "Longitudinal assessment of spinal cord injuries in nonhuman primates with quantitative magnetization transfer," *Magnetic resonance in medicine,* vol. 75, pp. 1685-1696, 2016.

[10] V. L. Yarnykh, "Fast macromolecular proton fraction mapping from a single off-resonance magnetization transfer measurement," *Magnetic resonance in medicine,* vol. 68, pp. 166-178, 2012.

[11] V. L. Yarnykh, "Time-efficient, high-resolution, whole brain three-dimensional macromolecular proton fraction mapping," *Magnetic resonance in medicine,* vol. 75, pp. 2100-2106, 2016.

[12] R. D. Dortch, F. Bagnato, D. F. Gochberg, J. C. Gore, and S. A. Smith, "Optimization of selective inversion recovery magnetization transfer imaging for macromolecular content mapping in the human brain," *Magnetic resonance in medicine,* 2018.
[13] A. K. Smith, S. By, B. D. Lyttle, R. D. Dortch, B. A. Box, L. J. Mckeithan*, et al.*, "Evaluating single-point quantitative magnetization transfer in the cervical spinal cord: Application to multiple sclerosis," *NeuroImage: Clinical,* vol. 16, pp. 58-65, 2017.
[14] G. B. Pike, "Pulsed magnetization transfer contrast in gradient echo imaging: A two-pool analytic description of signal response," *Magnetic resonance in medicine,* vol. 36, pp. 95-103, 1996.
[15] J. G. Sled and G. B. Pike, "Quantitative interpretation of magnetization transfer in spoiled gradient echo MRI sequences," *Journal of Magnetic Resonance,* vol. 145, pp. 24-36, 2000.
[16] S. Portnoy and G. J. Stanisz, "Modeling pulsed magnetization transfer," *Magnetic Resonance in Medicine,* vol. 58, pp. 144-155, 2007.
[17] G. Helms and G. E. Hagberg, "In vivo quantification of the bound pool T1 in human white matter using the binary spin–bath model of progressive magnetization transfer saturation," *Physics in Medicine & Biology,* vol. 54, p. N529, 2009.
[18] D. F. Gochberg and J. C. Gore, "Quantitative magnetization transfer imaging via selective inversion recovery with short repetition times," *Magnetic resonance in medicine,* vol. 57, pp. 437-441, 2007.
[19] M. Soellinger, C. Langkammer, T. Seifert-Held, F. Fazekas, and S. Ropele, "Fast bound pool fraction mapping using stimulated echoes," *Magnetic resonance in medicine,* vol. 66, pp. 717-724, 2011.
[20] G. Helms, "Interaction of exchange and differential relaxation in the saturation recovery behavior of the binary spin-bath model for magnetization transfer," *Concepts in Magnetic Resonance Part A: An Educational Journal,* vol. 28, pp. 291-298, 2006.
[21] C. Morrison and R. Mark Henkelman, "A model for magnetization transfer in tissues," *Magnetic resonance in medicine,* vol. 33, pp. 475-482, 1995.
[22] J. G. Sled and G. B. Pike, "Quantitative imaging of magnetization transfer exchange and relaxation properties in vivo using MRI," *Magnetic resonance in medicine,* vol. 46, pp. 923-931, 2001.
[23] S. Ropele, T. Seifert, C. Enzinger, and F. Fazekas, "Method for quantitative imaging of the macromolecular 1H fraction in tissues," *Magnetic Resonance in Medicine: An Official Journal of the International Society for Magnetic Resonance in Medicine,* vol. 49, pp. 864-871, 2003.
[24] G. Helms and A. Piringer, "Simultaneous measurement of saturation and relaxation in human brain by repetitive magnetization transfer pulses," *NMR in Biomedicine: An International Journal Devoted to the Development and Application of Magnetic Resonance In vivo,* vol. 18, pp. 44-50, 2005.
[25] I. Zelinka, "SOMA—self-organizing migrating algorithm," in *New optimization techniques in engineering*, ed: Springer, 2004, pp. 167-217.
[26] D. C. Alexander, "A general framework for experiment design in diffusion MRI and its application in measuring direct tissue-microstructure features," *Magnetic Resonance in Medicine,* vol. 60, pp. 439-448, 2008.
[27] M. Battiston, F. Grussu, A. Ianus, T. Schneider, F. Prados, J. Fairney*, et al.*, "An optimized framework for quantitative magnetization transfer imaging of the cervical spinal cord in vivo," *Magnetic resonance in medicine,* vol. 79, pp. 2576-2588, 2018.
[28] M. A. Bernstein, K. F. King, and X. J. Zhou, *Handbook of MRI pulse sequences*: Elsevier, 2004.

[29] R. Ordidge, P. Gibbs, B. Chapman, M. Stehling, and P. Mansfield, "High-speed multislice T1 mapping using inversion-recovery echo-planar imaging," *Magnetic resonance in medicine,* vol. 16, pp. 238-245, 1990.

[30] M. Garwood and L. DelaBarre, "The return of the frequency sweep: designing adiabatic pulses for contemporary NMR," *Journal of magnetic resonance,* vol. 153, pp. 155-177, 2001.

[31] R. Stollberger and P. Wach, "Imaging of the active B1 field in vivo," *Magnetic Resonance in Medicine,* vol. 35, pp. 246-251, 1996.

[32] M. J. Cardoso, M. Modat, R. Wolz, A. Melbourne, D. Cash, D. Rueckert*, et al.*, "Geodesic information flows: spatially-variant graphs and their application to segmentation and fusion," *IEEE transactions on medical imaging,* vol. 34, pp. 1976-1988, 2015.

[33] V. L. Yarnykh, "Pulsed Z-spectroscopic imaging of cross-relaxation parameters in tissues for human MRI: Theory and clinical applications," *Magnetic resonance in medicine,* vol. 47, pp. 929-939, 2002.

[34] A. Pampel, D. K. Müller, A. Anwander, H. Marschner, and H. E. Möller, "Orientation dependence of magnetization transfer parameters in human white matter," *NeuroImage,* vol. 114, pp. 136-146, 2015.

[35] G. Varma, G. Duhamel, C. de Bazelaire, and D. C. Alsop, "Magnetization transfer from inhomogeneously broadened lines: a potential marker for myelin," *Magnetic resonance in medicine,* vol. 73, pp. 614-622, 2015.

[36] G. Helms, H. Dathe, K. Kallenberg, and P. Dechent, "High-resolution maps of magnetization transfer with inherent correction for RF inhomogeneity and T1 relaxation obtained from 3D FLASH MRI," *Magnetic resonance in medicine,* vol. 60, pp. 1396-1407, 2008.

[37] N. Weiskopf, J. Suckling, G. Williams, M. M. Correia, B. Inkster, R. Tait*, et al.*, "Quantitative multi-parameter mapping of R1, PD*, MT, and R2* at 3T: a multi-center validation," *Frontiers in neuroscience,* vol. 7, p. 95, 2013.

[38] P. B. Kingsley, R. J. Ogg, W. E. Reddick, and R. G. Steen, "Correction of errors caused by imperfect inversion pulses in MR imaging measurement of T1 relaxation times," *Magnetic resonance imaging,* vol. 16, pp. 1049-1055, 1998.

[39] M. Boudreau, C. L. Tardif, N. Stikov, J. G. Sled, W. Lee, and G. B. Pike, "B1 mapping for bias-correction in quantitative T1 imaging of the brain at 3T using standard pulse sequences," *Journal of Magnetic Resonance Imaging,* vol. 46, pp. 1673-1682, 2017.

[40] J. L. Andersson, S. Skare, and J. Ashburner, "How to correct susceptibility distortions in spin-echo echo-planar images: application to diffusion tensor imaging," *Neuroimage,* vol. 20, pp. 870-888, 2003.

[41] J. Gomori, G. Holland, R. Grossman, W. Gefter, and R. Lenkinski, "Fat suppression by section-select gradient reversal on spin-echo MR imaging. Work in progress," *Radiology,* vol. 168, pp. 493-495, 1988.

[42] I. Levesque, J. G. Sled, S. Narayanan, A. C. Santos, S. D. Brass, S. J. Francis*, et al.*, "The role of edema and demyelination in chronic T1 black holes: a quantitative magnetization transfer study," *Journal of Magnetic Resonance Imaging: An Official Journal of the International Society for Magnetic Resonance in Medicine,* vol. 21, pp. 103-110, 2005.

[43] S. Mchinda, G. Varma, V. H. Prevost, A. Le Troter, S. Rapacchi, M. Guye*, et al.*, "Whole brain inhomogeneous magnetization transfer (ihMT) imaging: Sensitivity enhancement within a steady-state gradient echo sequence," *Magnetic resonance in medicine,* vol. 79, pp. 2607-2619, 2018.

[44] G. Varma, O. Girard, V. Prevost, A. Grant, G. Duhamel, and D. Alsop, "Interpretation of magnetization transfer from inhomogeneously broadened lines (ihMT) in tissues as a dipolar order effect within motion restricted molecules," *Journal of Magnetic Resonance,* vol. 260, pp. 67-76, 2015.

Figure 1: Pulse sequence diagram used in this study. An initial period of off-resonance saturation drives the system into steady-state and precedes the acquisition of a set of N_s slices, using a ssh-SE-EPI readout, while the saturation pulse continues to be played out. A key parameter of the sequence is the pulse repetition time $T=\tau+\Delta t$, where τ and Δt are the pulse duration and pulse gap respectively. As shown in the theory section of this paper, the steady-state created by MT pulse off-resonance saturation pulses at long T is insensitive to the exchange rate, enabling model approximations, as well as faster sampling of the steady-state (with single-shot EPI readouts). The property of the steady-state of being completely defined by the saturation parameters, and as such of being independent from the initial state of the system, allows the use of a short recovery time T_{rec} in between sequence repetitions.

Figure 2: Simulated percentage error distributions on model parameters *BPF* (in blue) and T_2^B (in yellow) at various *SNR* levels. The edges of the boxes represent the 25th and 75th distribution percentiles, while lines span from the 10th to the 90th distribution percentiles. Performance of all 6 protocols defined in Table 1 are shown. Large errors on the *BPF* are expected when conditions on the pulse repetition time are not met, as shown by protocol L1 having T=50ms, at all *SNR* levels. Black arrows indicate the optimized protocol O1, used for in vivo acquisition in this study. Despite a low number of data points M=10 (half of those used for long protocols L1, L2, L3 and L4), in the optimized protocol the *BPF* error is comparable to the longer ones, while the T_2^B error is effectively reduced.

Figure 3: Comparison of simulated protocols using synthetic parameter maps as a reference. Parameter maps in the first column (e.g. *BPF*, T_2^F, T_2^B, k_{FB} and T_1^{obs}) are used to simulate MT-weighted signals with the full Bloch equations, for a long protocol (L3 of table 1), a short protocol (S1 of table 1) and an optimized protocol (O1 of table 1). The approximated model is used to fit simulated signals and estimate *BPF* and T_2^B without making any hypotheses regarding the underlying k_{FB} and T_2^F, other than the fast-exchange assumption. The effects of *SNR*, number of data points and sampling optimization are readily appreciable from comparison of estimated parameter maps.

Figure 4: Examples of parameters maps in three different slices for a representative subject. T_1 maps are obtained from the IR acquisition (~4 minutes scan time), and plugged into the steady-state MT model to extract *BPF* and T_2^B from the MT-w ssh-SE-EPI acquisition (~4 minutes scan time). The *BPF* highlights differences between more myelinated WM and less myelinated GM structures. Higher variability within WM is instead displayed by T_2^B.

Figure 5: *BPF* maps 2mm isotropic resolution over 12cm of the human brain in a representative healthy subject, including B_1 correction. The total acquisition time (i.e. T_1 mapping + B_1 mapping + steady-state MT-weighted sequence, all using ssh-SE-EPI) to obtain these maps is less than 9 minutes.

Figure 6: *BPF* distributions from all subjects pooled together, with sub-distributions within each tissue-type: cortical grey matter (in red, cGM), white matter (in blue, WM), deep grey matter (in brown, dGM) and brain stem (in green, BS). The overall distribution (dashed black line) is bi-modal, with two distinct peaks corresponding to white matter and cortical grey matter, shown in panel a. Normalized distributions, shown in panel b, emphasize smaller structures, such as deep grey matter and brain stem. Deep grey matter is characterized by a higher median value compared to cGM, 0.074 vs 0.068.

Figure 7: Comparison between the fast steady-state approach developed here and a standard pulsed off-resonance qMT approach in the same single slice in one subject. The correlation between *BPF* estimates is high as shown by parametric maps, voxel wise scatter plots, and Bland-Altman plot within the selected slice. Different tissue types are visualized with different colours: cortical grey matter in red, white matter in blue, and deep grey matter in brown; the white dashed line represents the identity line. Comparison of T_2^B is less satisfactory (the correlation index and slope of linear regression between the fast approach and single slice off resonance qMT are lower compared to the ones obtained for BPF), however bias is limited (percentage error distribution median is -1.6%) and a similar spatial pattern can be observed in the parametric map, despite a noisier estimation.

Figure 8: Application to a SPMS case. Four example slices are shown in different rows, displaying different types of weighting obtained with a multi-contrast clinical protocol. From left to right: MPRAGE T_1-weighted scan, axial turbo spin-echo T_1-weighted scan, 3D turbo spin-echo T_2-weighted scan and 3D FLAIR scan. The co-localized BPF maps are shown in the last column. Abnormalities, such as WM lesions, in the clinical scans are indicated by red arrows. Such areas correspond to contrast variations in the BPF maps, showing focal changes surrounded by areas of more mild widespread *BPF* reductions. Quantitative *BPF* values in lesions and different tissue types are reported in the results section.

Table 1. Summary of sequence parameters for the MT-w protocols compared through simulations. *M*: number of data points; *T*: off-resonance pulse repetition time; τ: pulse duration; θ: flip angle of off-resonance saturation; Δ: offset frequency for off-resonance saturation.

	Protocol					
	L1	**L2**	**L3**	**L4**	**S1**	**O1**
M	20	20	20	20	8	10
T [ms]	50	100	150	200	150	150
$\boldsymbol{\tau}$ [ms]	6	6	6	6	6	8
$\boldsymbol{\theta}$ [°]	350/350/350/ 350/350/350/ 575/575/575/ 575/575/575/ 700/700/700/ 700/700/700/ 700/700	350/350/350/ 350/350/350/ 575/575/575/ 575/575/575/ 700/700/700/ 700/700/700/ 700/700	/350/350/350/ 350/350/350/ 575/575/575/ 575/575/575/ 700/700/700/ 700/700/700/ 700/700	/350/350/350/ 350/350/350/ 575/575/575/ 575/575/575/ 700/700/700/ 700/700/700/ 700/700	575/575/575/ 700/700/700/ 700/700	1000/600/ 1000/1000/ 600/1000/ 1000/600/ 1000/1000
Δ [kHz]	3/4/5/6/7/10/ 3/3.5/4/4.5/ 7.5/11/3/3.2/ 4/4.2/5/6.2/ 7.5/12	3/4/5/6/7/10/ 3/3.5/4/4.5/ 7.5/11/3/3.2/ 4/4.2/5/6.2/ 7.5/12	3/4/5/6/7/10/ 3/3.5/4/4.5/ 7.5/11/3/3.2/ 4/4.2/5/6.2/ 7.5/12	3/4/5/6/7/10/ 3/3.5/4/4.5/ 7.5/11/3/3.2/ 4/4.2/5/6.2/ 7.5/12	3/5/8/3/3.5/ 4/6/9	3/14.1/3/3/ 14.1/14.1/3/ 14.1/3/14.1

Table 2. Regional *BPF* values and inter-quartiles range in six healthy subjects, S1-S6.

	Region of interest			
	cortical grey matter	**deep grey matter**	**white matter**	**brain stem**
S1	0.071 (0.057-0.088)	0.080 (0.070-0.093)	0.124 (0.110-0.137)	0.092 (0.073-0.110)
S2	0.058 (0.045-0.073)	0.065 (0.056-0.074)	0.098 (0.086-0.107)	0.072 (0.056-0.088)
S3	0.068 (0.055-0.086)	0.077 (0.066-0.089)	0.113 (0.098-0.127)	0.084 (0.039-0.102)
S4	0.068 (0.053-0.085)	0.075 (0.065-0.087)	0.117 (0.103-0.129)	0.094 (0.079-0.110)
S5	0.071 (0.055-0.90)	0.076 (0.065-0.089)	0.121 (0.107-0.133)	0.092 (0.071-0.112)
S6	0.072 (0.058-0.088)	0.074 (0.064-0.085)	0.114 (0.102-0.125)	0.095 (0.077-0.112)
population average	0.068 (0.054-0.085)	0.075 (0.064-0.087)	0.114 (0.100-0.128)	0.088 (0.068-0.107)

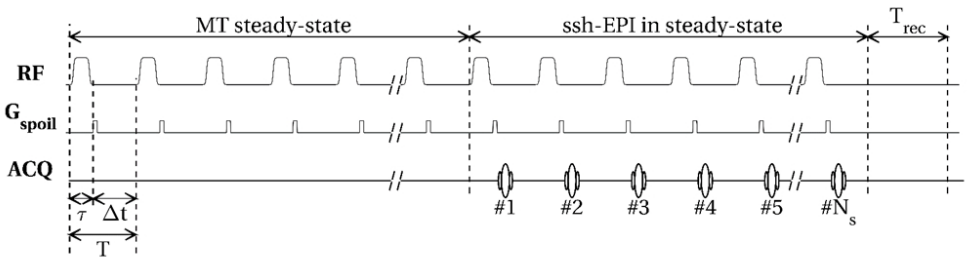

Figure 1: Pulse sequence diagram used in this study. An initial period of off-resonance saturation drives the system into steady-state and precedes the acquisition of a set of N_s slices, using a ssh-SE-EPI readout, while the saturation pulse continues to be played out. A key parameter of the sequence is the pulse repetition time $T=\tau+\Delta t$, where τ and Δt are the pulse duration and pulse gap respectively. As shown in the theory section of this paper, the steady-state created by MT pulse off-resonance saturation pulses at long T is insensitive to the exchange rate, enabling model approximations, as well as faster sampling of the steady-state (with single-shot EPI readouts). The property of the steady-state of being completely defined by the saturation parameters, and as such of being independent from the initial state of the system, allows the use of a short recovery time T_{rec} in between sequence repetitions.

86x26mm (300 x 300 DPI)

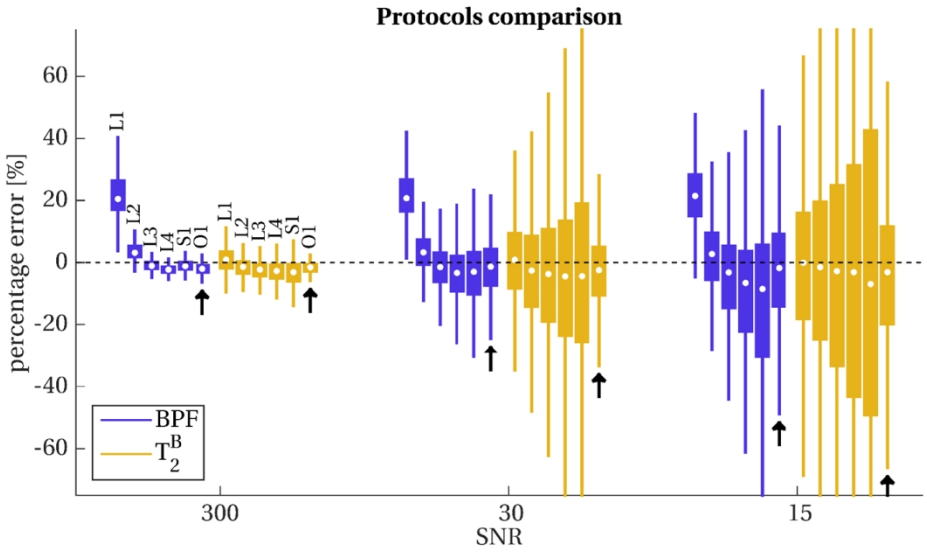

Figure 2: Simulated percentage error distributions on model parameters *BPF* (in blue) and T_2^B (in yellow) at various *SNR* levels. The edges of the boxes represent the 25th and 75th distribution percentiles, while lines span from the 10th to the 90th distribution percentiles. Performance of all 6 protocols defined in Table 1 are shown. Large errors on the *BPF* are expected when conditions on the pulse repetition time are not met, as shown by protocol L1 having T=50ms, at all *SNR* levels. Black arrows indicate the optimized protocol O1, used for in vivo acquisition in this study. Despite a low number of data points M=10 (half of those used for long protocols L1, L2, L3 and L4), in the optimized protocol the *BPF* error is comparable to the longer ones, while the T_2^B error is effectively reduced.

130x74mm (300 x 300 DPI)

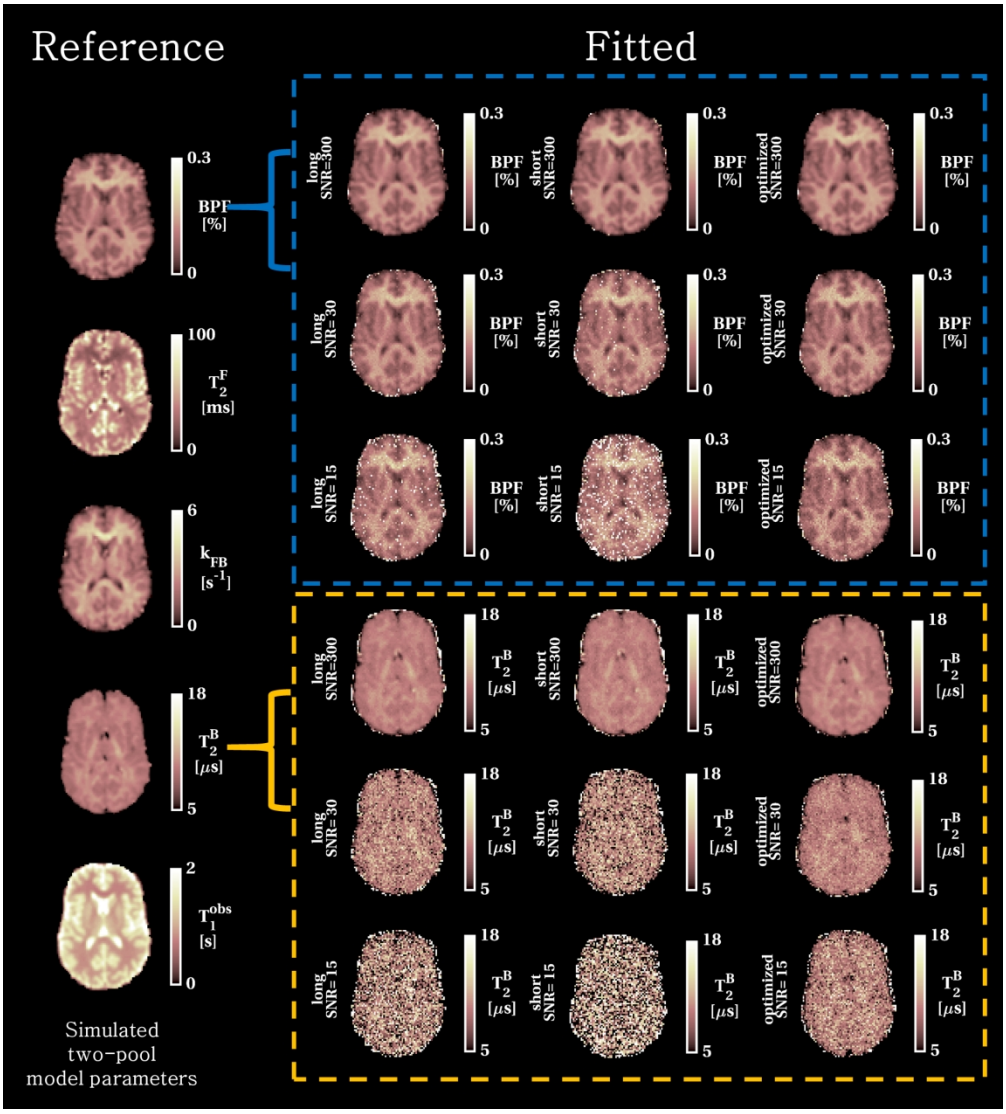

Figure 3: Comparison of simulated protocols using synthetic parameter maps as a reference. Parameter maps in the first column (e.g. *BPF*, T_2^F, T_2^B, k_{FB} and T_1^{obs}) are used to simulate MT-weighted signals with the full Bloch equations, for a long protocol (L3 of table 1), a short protocol (S1 of table 1) and an optimized protocol (O1 of table 1). The approximated model is used to fit simulated signals and estimate *BPF* and T_2^B without making any hypotheses regarding the underlying k_{FB} and T_2^F, other than the fast-exchange assumption. The effects of *SNR*, number of data points and sampling optimization are readily appreciable from comparison of estimated parameter maps.

175x193mm (300 x 300 DPI)

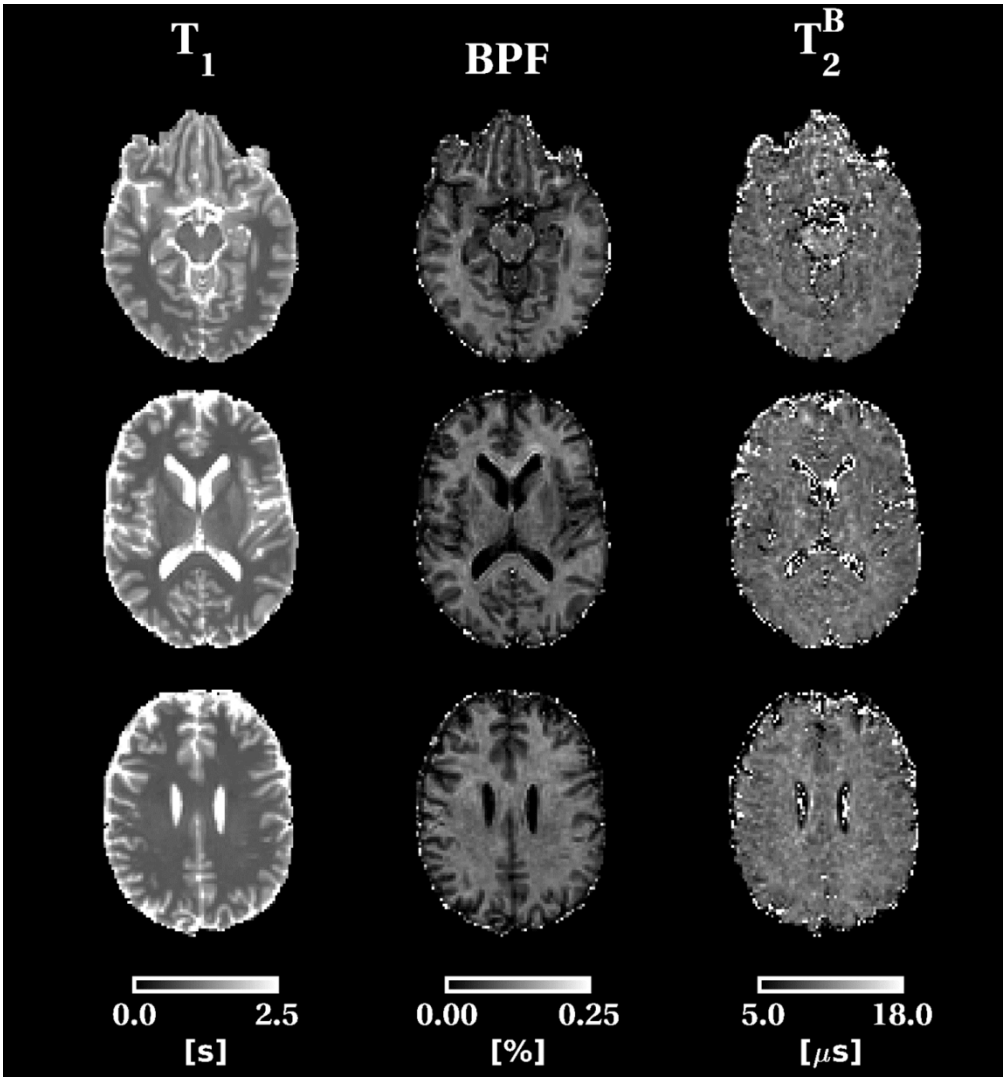

Figure 4: Examples of parameters maps in three different slices for a representative subject. T_1 maps are obtained from the IR acquisition (~4 minutes scan time), and plugged into the steady-state MT model to extract *BPF* and T_2^B from the MT-w ssh-SE-EPI acquisition (~4 minutes scan time). The *BPF* highlights differences between more myelinated WM and less myelinated GM structures. Higher variability within WM is instead displayed by T_2^B.

130x139mm (300 x 300 DPI)

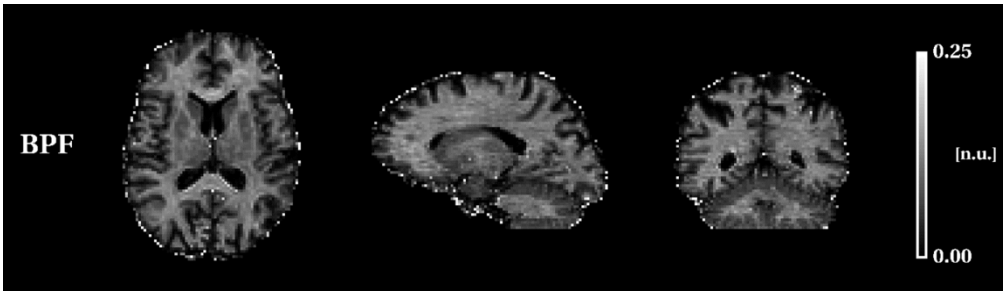

Figure 5: *BPF* maps 2mm isotropic resolution over 12cm of the human brain in a representative healthy subject, including B_1 correction. The total acquisition time (i.e. T_1 mapping + B_1 mapping + steady-state MT-weighted sequence, all using ssh-SE-EPI) to obtain these maps is less than 9 minutes.

175x50mm (300 x 300 DPI)

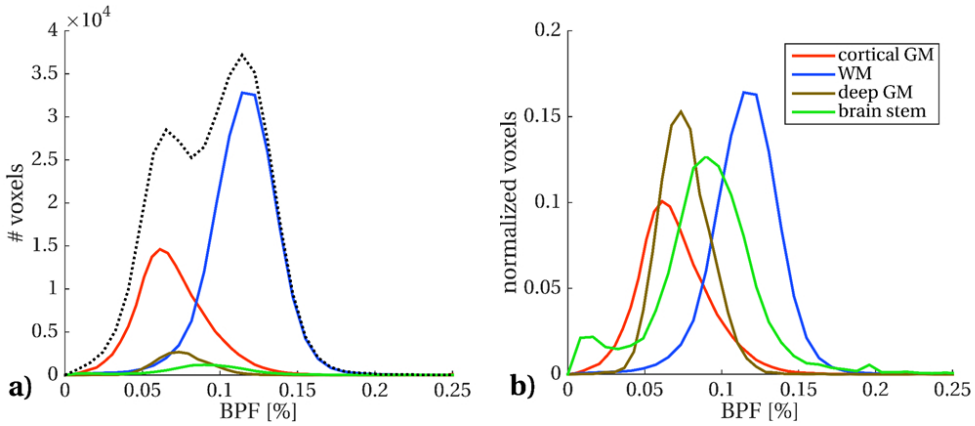

Figure 6: *BPF* distributions from all subjects pooled together, with sub-distributions within each tissue-type: cortical grey matter (in red, cGM), white matter (in blue, WM), deep grey matter (in brown, dGM) and brain stem (in green, BS). The overall distribution (dashed black line) is bi-modal, with two distinct peaks corresponding to white matter and cortical grey matter, shown in panel a. Normalized distributions, shown in panel b, emphasize smaller structures, such as deep grey matter and brain stem. Deep grey matter is characterized by a higher median value compared to cGM, 0.074 vs 0.068.

86x36mm (300 x 300 DPI)

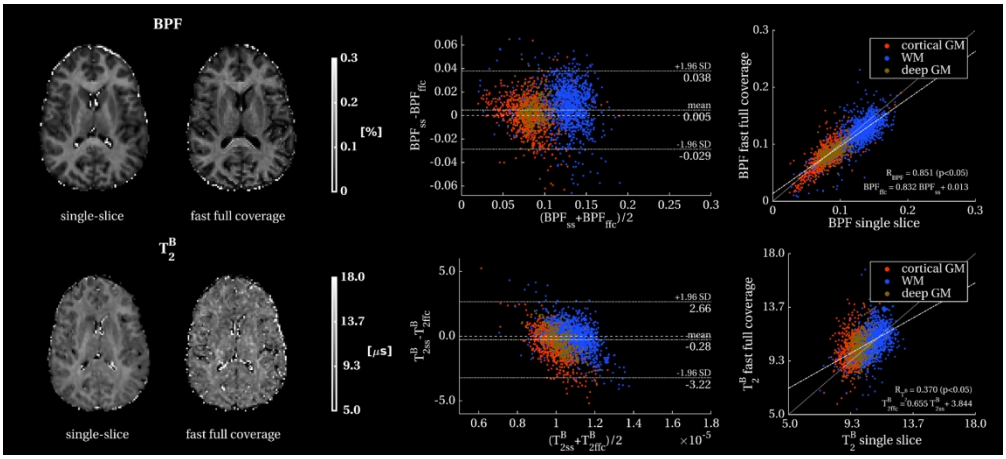

Figure 7: Comparison between the fast steady-state approach developed here and a standard pulsed off-resonance qMT in the same single slice in one subject. The correlation between *BPF* estimates is high as shown by parametric maps, voxel wise scatter plots, and Bland-Altman plot within the selected slice. Different tissue types are visualized with different colours: cortical grey matter in red, white matter in blue, and deep grey matter in brown; the white dashed line represents the identity line. Comparison of T_2^B is less satisfactory (the correlation index and slope of linear regression between the fast approach and single slice off resonance qMT are lower compared to the ones obtained for *BPF*), however bias is limited (percentage error distribution median is -1.6%) and a similar spatial pattern can be observed in the parametric map, despite a noisier estimation.

175x79mm (300 x 300 DPI)

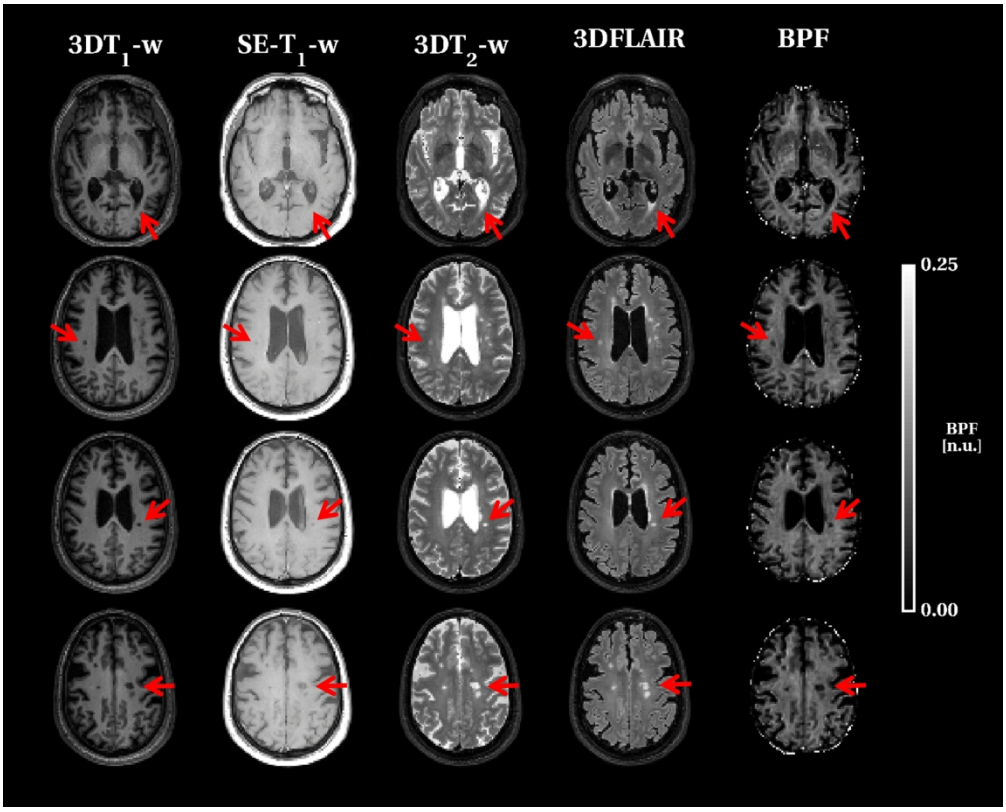

Figure 8: Application to a SPMS case. Four example slices are shown in different rows, displaying different types of weighting obtained with a multi-contrast clinical protocol. From left to right: MPRAGE T_1-weighted scan, axial turbo spin-echo T_1-weighted scan, 3D turbo spin-echo T_2-weighted scan and 3D FLAIR scan. The co-localized *BPF* maps are shown in the last column. Abnormalities, such as WM lesions, in the clinical scans are indicated by red arrows. Such areas correspond to contrast variations in the *BPF* maps, showing focal changes surrounded by areas of more mild widespread *BPF* reductions. Quantitative *BPF* values in lesions and different tissue types are reported in the results section.

175x140mm (300 x 300 DPI)

Fast bound pool fraction mapping via steady-state magnetization transfer saturation using single-shot EPI

Manuscript # MRM-18-19687

Supporting information

Supporting Information Figure S1

Details of imaging and preparation pulses used in the optimized in vivo acquisition: slice selective excitation pulse (a), slice selective refocusing pulse (b), off-resonance saturation Fermi pulse (c), and hyperbolic secant adiabatic inversion pulse (d). In the in vivo MT-weighted acquisition, the Fermi pulse is used at two different amplitudes (following protocol optimization), $B_{1,max}$=10.8μT and $B_{1,max}$=7.95 μT, with the same duration τ=8ms.

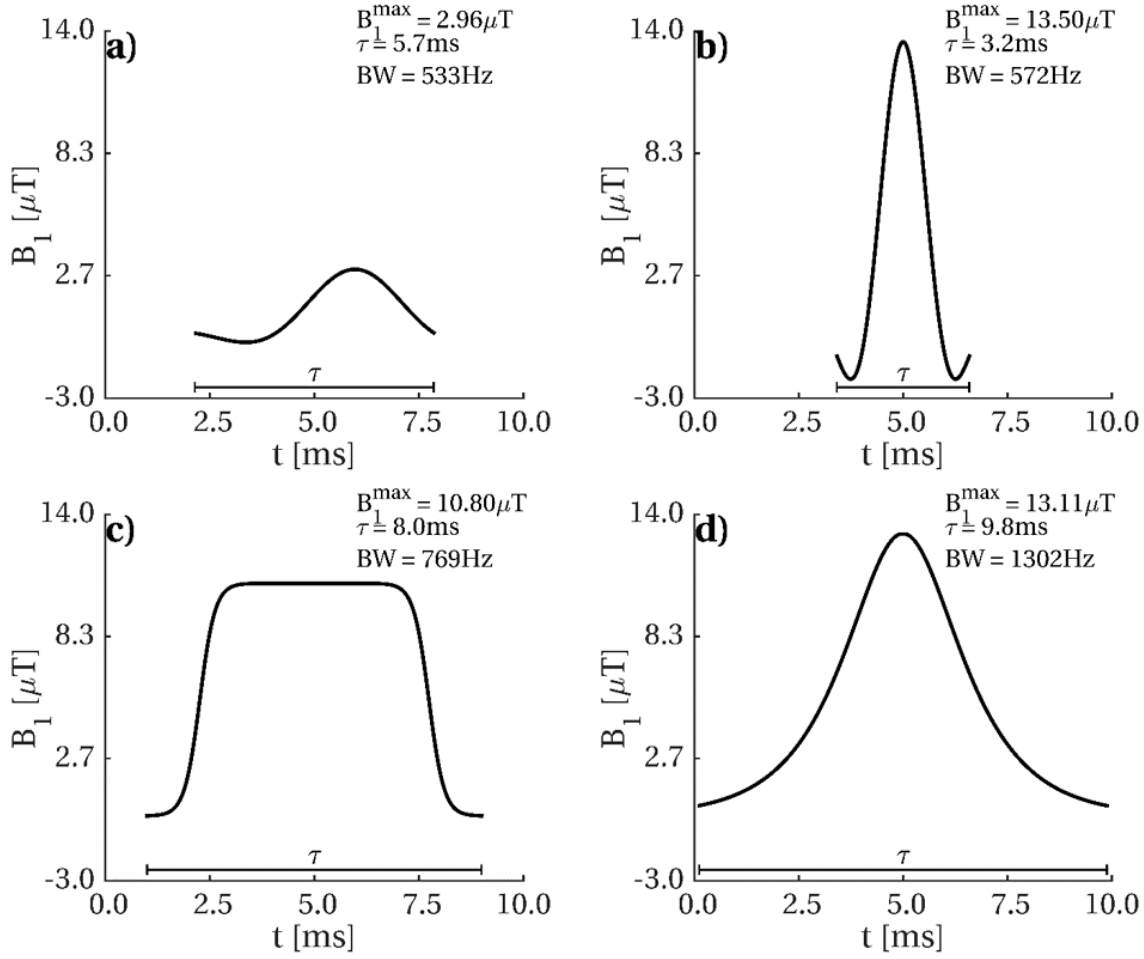

Supporting Information Figure S2

Fast exchange model approximations. Different exchange regimes are analysed by artificially varying k_{FB}, starting from the model parameter configuration used in the simulations section shown in Figure 3. Faster exchange regimes correspond to lower values of ε (defined by equation 6), as shown in panel a. The exchange regime measured in vivo in the single slice qMT reference acquisition (described in the methods section) is reported in all the graphs (blue dashed line, which refers to the median of the distribution within the single slice). Validity of conditions $D \approx 0$ (panel b), $K \approx BPF$ (panel c), and $e^{-(\lambda_2-\lambda_1)T} \approx 0$ for T=100ms, 150ms and 200ms (panel c) are investigated at varying ε. In panel e) the overall effect on BPF estimation is analysed using the sampling protocols L2, L3 and L4 of table 2 as reference, at SNR=300. The use of long T (e.g. T =150ms) allows to maintain the percentage BPF error below 10% even at exchange regimes characterized by ε=0.02 (compared to a measured in vivo exchange regime ε=0.012). Median and interquartile ranges are reported in simulated trends.

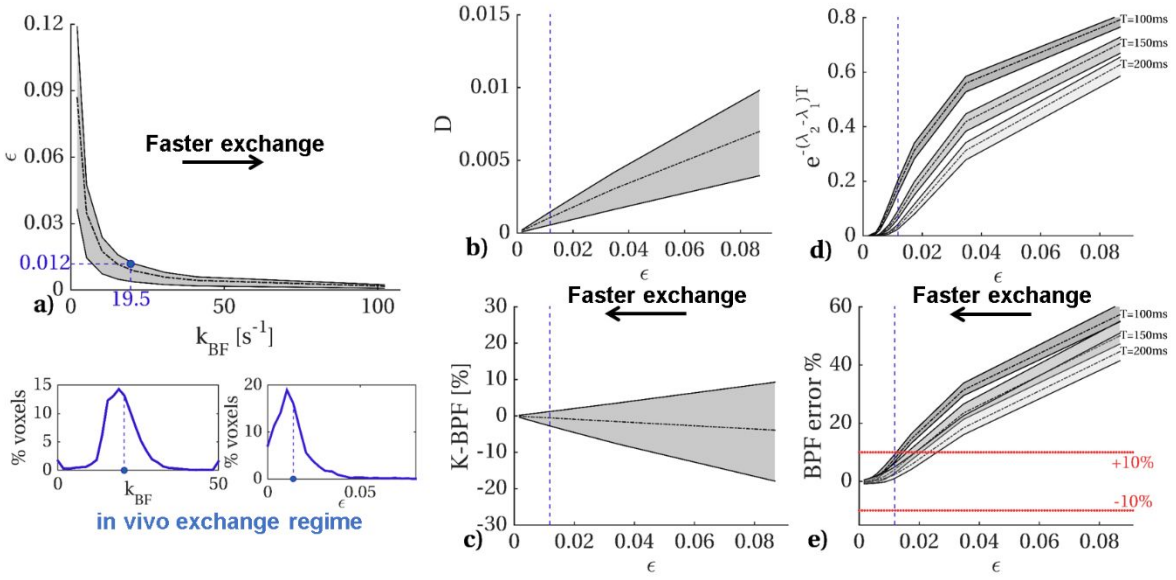

Supporting Information Figure S3

Effect of the multislice acquisition module on model parameter estimates. Full two-pool Bloch equations are used to simulated MT-weighted signal of the optimized protocol O1, accounting also for additional off-resonance saturation via slice selective imaging pulses of the multislice SE-EPI readout. For each slice index i=1,…,N_s, the set of offset frequencies of excitation and refocusing pulses are obtained as $\gamma G \Delta z_{t,i}$ where G is the slice selective gradient strength, and $\Delta z_{i,t}$ is the space gap between slice i and any slice t=1,..,i-1 that precedes slice i in the acquisition. The odd-even slice acquisition order used for in vivo acquisition is reproduced in the simulation, and realistic shapes are used for the imaging pulses and preparation pulses (see Supporting Information Figure S1). The approximated model proposed is used to fit the simulated data, and percentage error on *BPF* and T_2^B is evaluated at varying *SNR*. Incidental MT-weighting from imaging spin echo pulses has a severe impact on the accuracy of *BPF* estimates, while T_2^B is less affected (*odd-even* boxplots). Prior to model fitting, however, MT-weighted images are normalized to a reference image, i.e. M_0, which is acquired within the same sequence (hence similarly affected by MT-weighting via imaging pulses). The normalization with such an M_0 image greatly attenuate the error on *BPF* estimates (*odd-even normalized* boxplots), resulting in a median percentage error of 12.3%, 12.1% and 11.9% at *SNR*=300, 30 and 15 respectively.

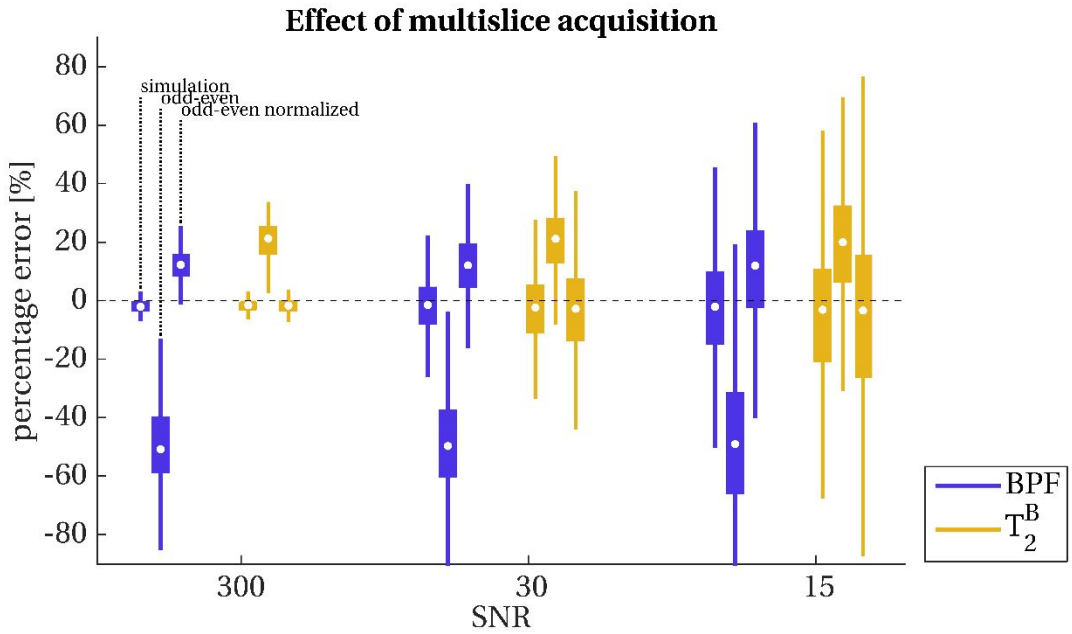

Supporting Information Figure S4

Axial views of *BPF* maps at 2mm in plane resolution in a representative healthy subject, including B_1 correction. The total acquisition time (i.e. T_1 mapping + B_1 mapping + steady-state MT-weighted sequence, all using ssh-SE-EPI) to obtain these maps is less than 9 minutes.

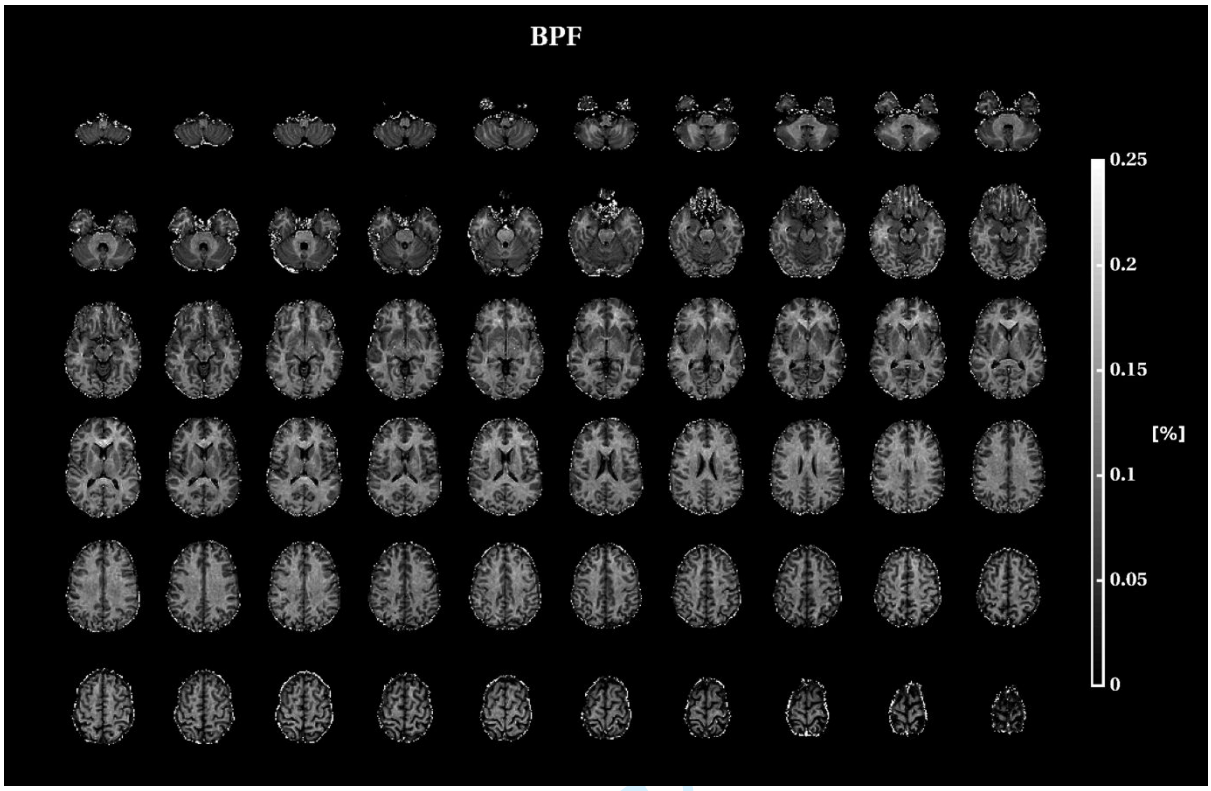

Supporting Information Figure S5

Analysis of error propagation from T_1 measurements to *BPF* estimates, following imperfect inversion of the hyperbolic secant adiabatic inversion pulse used in the IR-EPI sequence. Inversion Recovery curves are simulated at varying inversion efficiency β=0.85, 0.9, 0.95 and 1, and then fitted with a standard 2-parameter (where unknown model parameters are M_0 and T_1^{obs}), and a 3-parameter model (where unknown model parameters are M_0, $T_1^{obs}=1/R_1^{obs}$, and β). The R_1^{obs} estimates obtained are then used as input in the qMT model for *BPF* and T_2^B estimation. Percentage errors are reported for both IR-EPI fitting approaches (2-parameter fitting in box a, and 3-parameter fitting in b). The optimized protocol proposed for the in vivo acquisition (O1) is used to generate simulated MT-weighted data.